fluids

MDPI

Article

Apparent Hamaker Constants and Characteristic Interaction Distances Governing Sol–Gel Transitions in Aqueous Smectite Clay Dispersions

Hiroshi Kimura [1,*], Haruka Tanabe [2] and Susumu Shinoki [2]

[1] Department of Chemistry and Biomolecular Science, Faculty of Engineering, Gifu University, Gifu 501-1193, Japan
[2] Development Division, Iwaki Laboratories, KUNIMINE INDUSTRIES Co., Ltd., Fukushima 972-8312, Japan; haruka_tanabe@kunimine.co.jp (H.T.); shinoki-s44@kunimine.co.jp (S.S.)
* Correspondence: kimura.hiroshi.b1@f.gifu-u.ac.jp

Abstract

Aqueous smectite clay dispersions undergo sol–gel transitions and form three-dimensional networks at relatively low clay concentrations. However, the clay and electrolyte concentrations required for gelation differ markedly among clay species, and the physical origin of these differences remains unclear. In this study, sol–gel state diagrams were constructed for four smectite clays based on rheological measurements, and DLVO analysis was subsequently applied to the experimentally determined sol–gel transition boundaries using the corresponding zeta potentials and Debye lengths. The apparent Hamaker constant, $A_{H,app}$, decreased with increasing NaCl concentration for all clays. In addition, $\ln(A_{H,app}/10^{-20}\ J)$ showed approximately linear relationships with the reciprocal Debye length, $1/L_D$, with distinct trends in the low- and high-salt regions. A characteristic interaction distance, H^*, was defined as the negative of the fitted slope. H^* was larger and more strongly clay-dependent in the low-salt region, whereas it became smaller and less clay-dependent in the high-salt region. The crossover in H^*, observed at approximately 0.01–0.03 mol/L NaCl, occurred in the same broad concentration range as the onset of decreased transmittance and previously reported rheological changes. Because these datasets were acquired at non-identical clay volume fractions, this agreement should be regarded as qualitative rather than as a direct one-to-one correspondence.

Keywords: smectite clay; sol–gel transition; DLVO theory; apparent Hamaker constant; characteristic interaction distance; zeta potential; Debye length; colloidal gel

Check for updates

Academic Editor: Rajinder Pal

Received: 9 July 2026
Revised: 27 August 2026
Accepted: 7 September 2026
Published: 9 September 2026

Copyright: © 2026 by the authors. Licensee MDPI, Basel, Switzerland. This article is an open access article distributed under the terms and conditions of the Creative Commons Attribution (CC BY) license.

1. Introduction

Layered clay minerals, including smectites, have been studied in a wide range of fields, such as colloid science, geoscience, materials science, and chemical engineering, because of their high specific surface area, ion-exchange capacity, swelling ability, and anisotropic particle shape [1,2]. In particular, smectite clays form stable colloidal dispersions in water and exhibit various dispersed, aggregated, and self-assembled structures depending on conditions such as electrolyte concentration, pH, and clay concentration [3–6]. Therefore, they have been studied in relation to a broad range of applications, from understanding the mechanical properties and mass transport phenomena of soils and sediments to designing cosmetics, paints, drilling fluids, pharmaceutical and food materials, and functional soft materials [6–8].

One important feature of aqueous smectite clay dispersions is that they undergo sol–gel transitions and form three-dimensional network structures even at relatively low clay concentrations [9]. The formation of such networks gives rise to characteristic rheological properties, including yield stress, thixotropy, and storage elasticity [10–12]. Because these gels are physical gels formed through interparticle interactions without chemical crosslinking, they are regarded as representative model systems for understanding network formation mechanisms in anisotropic colloidal dispersions. In this paper, the dispersed units of smectites in water, including individual layers and tactoids, are referred to as "particles" for convenience.

Various models have been proposed to explain the gelation mechanisms of smectite dispersions. Representative examples include the house-of-cards structural model based on edge–face association [1,11,13,14], the percolation model based on anisotropic interparticle interactions [12], and the Wigner glass model, in which particle motion is suppressed by long-range electrostatic repulsion [15,16]. These studies indicate that the sol–gel transition of clay dispersions is not a simple aggregation phenomenon, but rather a hierarchical network formation process involving the combined effects of particle shape, surface charge, electric double layers, particle orientation, and local fluctuations in clay concentration.

The electrolyte and clay concentration conditions under which sol–gel transitions occur differ markedly among clay species, even within the same family of smectite clays. For example, gel formation has been reported in aqueous Laponite dispersions even at relatively low clay concentrations [3,5,10], whereas aggregation and gelation in aqueous montmorillonite and natural bentonite dispersions are known to occur under different conditions depending on the electrolyte and clay concentrations [7,17]. A recent review also pointed out that the gelation behavior of smectite clays differs substantially among clay species [9]. However, most previous studies have focused on a single clay species, and systematic comparisons of sol–gel transition boundaries over a wide range of electrolyte and clay concentrations under the same evaluation criteria remain limited. Therefore, why gelation conditions differ among clay species and what physical parameters govern these differences remain insufficiently understood.

Smectites dispersed in water have a high specific surface area and structurally fixed negative charges originating from their layered crystal structures. Consequently, electric double layers form around clay surfaces in water, giving rise to electrostatic repulsion between clay particles. Such interparticle interactions are often described by the Derjaguin–Landau–Verwey–Overbeek (DLVO) theory, which treats them as a balance between van der Waals attraction and electric double-layer repulsion [18–20]. DLVO theory has also been widely applied to the analysis of critical coagulation concentrations and aggregation kinetics in aqueous clay dispersions [17,21]. However, actual clay dispersions cannot always be fully described by a simple spherical-particle model, because factors such as strong particle-shape anisotropy, differences in charge characteristics between basal faces and edges, hydration, interlayer swelling, orientation-dependent association, and tactoid formation are involved [2,8,17].

To understand such complex network formation, it is important to focus not only on the strength of interparticle interactions but also on the characteristic length scales involved in network formation. Pignon et al. (1996) [22] showed that the characteristic length of fractal aggregates formed in Laponite gels is on the order of approximately 1 μm and reported that this length scale is closely related to macroscopic rheological properties such as yield stress. Similarly, characteristic lengths and heterogeneous structures in smectite gels have also been reported by SAXS and USAXS measurements [23]. These findings indicate that extracting the distance scales governing network formation is effective for understanding the sol–gel transitions and rheological properties of aqueous clay dispersions.

The authors have systematically investigated the gel transparency [24], rheological properties [25], drying patterns of sessile droplets [26], and electrorheological responses under low electric fields of up to several V/mm DC [27] for several deionized aqueous smectite clay dispersions. These studies revealed the clear clay-species dependence of these properties, and their order was found to correspond well to that of the zeta potential. In particular, the clay-species dependence of transmittance, yield stress, and dynamic viscoelastic properties showed strong correlations with the absolute value of the zeta potential [25]. These results indicate that the zeta potential is an important indicator reflecting the network-forming ability of clay dispersions.

On the other hand, the zeta potential is an indicator of the strength of electric double-layer repulsion and does not directly specify the distance scale over which interparticle interactions manifest as network formation. In other words, the zeta potential provides information on the "strength of interaction," but not on the "distance over which network formation effectively occurs." Therefore, to better understand the differences in sol–gel transition conditions and network formation mechanisms among clay species, a new approach is needed to evaluate not only the strength of interactions but also the distance scale over which these interactions act.

In this study, sol–gel state diagrams were constructed from rheological measurements for four smectite clays: fluorinated hectorite (Ht-F), stevensite (Stv), hectorite (Ht), and saponite (Sap). Furthermore, DLVO analysis was performed using the zeta potential and Debye length at the sol–gel transition boundary, and the apparent Hamaker constant, $A_{H,app}$, was evaluated. By analyzing the electrolyte-concentration dependence of $A_{H,app}$, an effective distance scale associated with network formation was extracted and defined as the characteristic interaction distance, H^*. In contrast to our previous studies, the present study directly focuses on the experimentally determined sol–gel transition boundaries and maps each transition condition onto $A_{H,app}$ within a DLVO-based framework. The electrolyte-concentration dependence of the resulting $A_{H,app}$ values is then used to determine H^*, thereby enabling the sol–gel transition behavior of different clay species to be compared on a common basis. The aim of this study is to examine whether H^* provides a useful effective parameter for comparing clay-species-dependent sol–gel transition behavior and network-forming states.

2. Materials and Methods

2.1. Materials and Sample Preparation

In this study, four synthetic smectite clay minerals supplied by KUNIMINE INDUSTRIES Co., Ltd. (Tokyo, Japan) were used: fluorinated hectorite (Ht-F), stevensite (Stv), hectorite (Ht), and saponite (Sap). The chemical compositions of the clays are as follows.

$$\text{Ht-F: } Na_{0.33}(Mg_{2.67}Li_{0.33})Si_4O_{10}(F,OH)_2$$

$$\text{Stv: } Na_{0.16}Mg_{2.92}Si_4O_{10}(OH)_2$$

$$\text{Ht: } Na_{0.33}(Mg_{2.67}Li_{0.33})Si_4O_{10}(OH)_2$$

$$\text{Sap: } Na_{0.33}Mg_3(Si_{3.67}Al_{0.33})O_{10}(OH)_2$$

Ht-F is a clay in which approximately 50% of the edge OH groups in Ht are replaced by fluorine atoms. Ht-F and Ht possess layer charges generated by partial substitution of Mg^{2+} by Li^+ in the octahedral sheet. In contrast, Stv has layer charges originating from Mg vacancies in the octahedral sheet. Sap has layer charges generated by partial substitution of Si^{4+} by Al^{3+} in the tetrahedral sheet. All four clays consist of thin platelet-like particles, and the thickness of a single nanosheet is approximately 1 nm. The cumulant mean diameters

(Stokes diameters) measured by dynamic light scattering (nanoPartica SZ-100 Z2, HORIBA, Kyoto, Japan) were 40, 46, 79, and 108 nm for Ht-F, Stv, Ht, and Sap, respectively [25]. The density of all clays was 2.5 g/cm^3. The specific surface areas estimated from these particle diameters and thicknesses were approximately 800 m^2/g for all clays, reflecting the extremely large specific surface area characteristic of smectites. The cation exchange capacity (CEC) was measured using a Quick Ammonia Meter AT-200 (Central Kagaku Corp., Tokyo, Japan), and the values were 70, 32, 49, and 70 meq/100 g for Ht-F, Stv, Ht, and Sap, respectively [25]. Thus, the four clays used in this study differ in particle size, CEC, and the origin of layer charge, making them suitable model systems for comparing clay-species-dependent behavior.

Deionized stock dispersions were prepared by first dispersing clay powders in ultrapure water (Milli-Q Advantage A10, Millipore Co., Burlington, MA, USA) under stirring, followed by the addition of mixed ion-exchange resin AG501-X8(D) (Bio-Rad Laboratories, Hercules, CA, USA) and deionization for more than 3 months. The volume fractions of the resulting stock dispersions were ϕ = 0.018–0.019. Experimental samples were prepared by diluting the deionized stock dispersions with ultrapure water and NaCl aqueous solutions. The clay volume fraction was varied from ϕ = 0.001 to 0.017, and the added salt concentration, [NaCl], was up to 0.1 mol/L.

Aqueous smectite clay dispersions are known to exhibit aging behavior, in which the zeta potential and rheological properties change with time [11,28–33]. Therefore, all samples were allowed to stand for at least 24 h after preparation. Both the zeta-potential and rheological measurements were performed using samples prepared according to the same procedure and within the same post-preparation age window, namely, after at least 24 h and within 1 week after preparation. Rheological measurements were performed after applying the prescribed pre-shear and allowing an approximately 3 min rest period. All experiments were conducted at 25 °C.

These standardized preparation histories and matched measurement-age windows were used to minimize systematic aging-related differences between the zeta-potential and rheological datasets. However, the measurements were not necessarily performed on the same aliquot or at exactly the same elapsed time, and the stability of the sol–gel boundary throughout the one-week measurement period was not independently evaluated. Therefore, residual aging effects cannot be completely excluded as a possible source of variation in the determined boundary points and the derived $A_{\mathrm{H,app}}$ and H^* values.

2.2. Zeta Potential Measurements

The zeta potential, ζ, was measured by electrophoretic light scattering using a Zetasizer Nano ZS (Malvern Panalytical Ltd., Malvern, UK). Measurements were performed at 25 °C for samples with volume fractions of ϕ = 0.001, 0.002, and 0.003 at various NaCl concentrations. It should be noted that, because the measured values may be affected by interparticle interactions near the sol–gel transition, the zeta potentials obtained in this study should be interpreted as apparent values under each measurement condition.

The relationship between the electrophoretic mobility, μ_{e}, and ζ is given by Henry's equation as follows:

$$\mu_{\mathrm{e}} = \frac{\varepsilon\zeta}{\eta} f(\kappa a). \quad (1)$$

Here, ε is the absolute permittivity of water (6.95×10^{-10} F/m), η is the viscosity of water (8.90×10^{-4} Pa·s), and κ is the Debye–Hückel parameter [20,34]. The parameter a

denotes the effective particle radius. In this study, the following approximate expression proposed by Ohshima, $f_{\mathrm{Ohshima}}(\kappa a)$, was used to calculate the Henry function $f(\kappa a)$ [35]:

$$f_{\mathrm{Ohshima}}(\kappa a) = \frac{2}{3}\left(1 + \frac{1}{2\left[1 + \frac{2.5}{\kappa a(1+2\exp(-\kappa a))}\right]^3}\right). \quad (2)$$

The Ohshima expression was selected because it provides a simple and accurate analytical approximation to Henry's function for spherical colloidal particles, with a reported relative error of less than 1% [35]. In addition, it allows continuous evaluation as a function of κa, avoiding the need to switch between the Hückel and Smoluchowski limiting expressions and enabling the same calculation procedure to be applied consistently to all clay samples.

The smectite clays used in this study are platelet-like particles, and their interparticle interactions strongly depend on particle orientation. The DLS cumulant diameter is obtained from translational diffusion through the Stokes–Einstein relation and represents the diameter of a sphere having equivalent hydrodynamic drag. For platelet-like and polydisperse clay populations, this quantity is not a direct measure of either the lateral dimension or thickness of an individual nanosheet and may also be influenced by particle orientation, aspect-ratio distribution, and the presence of tactoids or small aggregates. Its use as the effective particle diameter, d, in the Henry-function and sphere–sphere DLVO calculations therefore assumes, solely for comparative purposes, that each clay population can be represented by a single hydrodynamically equivalent sphere. This approximation provides a common analytical basis for internally consistent comparison among the four clay species, although the absolute values derived from the analysis may depend on the assumed effective size and particle geometry. Thus, the present results do not imply that particle-shape anisotropy is negligible.

The Debye–Hückel parameter, κ, was obtained as the reciprocal of the Debye length, L_{D}. For a 1:1 electrolyte aqueous solution at 25 °C, L_{D} (m) is given by the following equation [20,36]:

$$L_{\mathrm{D}} = \frac{3.04}{\sqrt{c}} \times 10^{-10} \quad (3)$$

where c is the NaCl concentration in mol/L. For the deionized condition ([NaCl] = 0), the effective electrolyte concentration was estimated to be $c = 1.0 \times 10^{-5}$ mol/L from the electrical conductivity of ultrapure water, and the corresponding Debye length was taken as L_{D} = 96 nm [37]. The value of ζ was calculated from the measured electrophoretic mobility using Equations (1)–(3).

2.3. Dynamic Rheological Measurements

Dynamic viscoelastic measurements were performed to determine the sol–gel transition boundary. The authors have previously reported sol–gel state diagrams based on dynamic viscoelastic measurements for aqueous dispersions of four smectite clays [24]. In the present study, additional measurements were carried out mainly in the ranges of clay volume fraction ϕ = 0.001–0.003 and added salt concentration [NaCl] = 0.005–0.10 mol/L to determine the sol–gel boundary in more detail. Dynamic viscoelastic measurements were performed using a double-cylinder rotational rheometer (Rheosol-G2000W-GF, UBM Co., Ltd., Kyoto, Japan). The gap between the inner and outer cylinders was 0.5 mm.

Before the measurements, all samples were subjected to pre-shear at 100 s^{-1} for 60 s and then allowed to stand for approximately 3 min. The strain amplitude was set to γ = 0.002. In the authors' previous study, γ = 0.002 was confirmed to be within the linear viscoelastic region even near the sol–gel transition; therefore, the same condition was

adopted in this study. First, the angular frequency dependence of the storage modulus, G', and loss modulus, G'', was examined for samples near the sol–gel transition in the range of approximately 0.02–0.2 rad/s. For these samples, no reversal between G' and G'' with changing angular frequency was observed. The sol–gel state was evaluated using the loss tangent, tan δ (=G''/G'). Samples with tan $\delta > 1$ were defined as being in the sol state, whereas those with tan $\delta < 1$ were defined as being in the gel state. Based on this criterion, sol–gel state diagrams were constructed for each aqueous clay dispersion.

2.4. Transmittance Measurements

The transmittance was measured using a laboratory-built apparatus [24]. A clay volume fraction of $\phi = 0.003$, which is near the sol–gel transition, was selected for the measurements. A rectangular glass cell with inner dimensions of 10.0 mm × 10.0 mm × 44.0 mm was used, and the optical path length was 10.0 mm. A He–Ne laser beam with a wavelength of 632.8 nm and a beam diameter of 0.5 mm was directed perpendicular to the cell wall, and the transmittance was measured. All measurements were performed at 25 °C.

2.5. DLVO Analysis

The interparticle interactions between clay particles in water were evaluated based on the Derjaguin–Landau–Verwey–Overbeek (DLVO) theory [18,19]. The total interaction potential, $V(H)$, was expressed as the sum of the electric double-layer repulsion term, $V_R(H)$, and the van der Waals attraction term, $V_A(H)$. For these terms, the following representative approximate expressions for interactions between spherical particles were used [36,38]:

$$V(H) = V_R(H) + V_A(H), \tag{4}$$

where H is the surface-to-surface separation between particles. The electric double-layer repulsion term, $V_R(H)$, was expressed as an exponentially decaying term:

$$V_R(H) = \frac{\pi d^2 \varepsilon \psi_0^2 \exp\left(-\frac{H}{L_D}\right)}{d + H}. \tag{5}$$

On the other hand, the van der Waals attraction term, $V_A(H)$, which is characterized by the Hamaker constant, was expressed as

$$V_A(H) = -\frac{A_H d}{24H} \tag{6}$$

where d is the effective particle diameter, ε is the absolute permittivity of water, ψ_0 is the particle surface potential, L_D is the Debye length, and A_H is the Hamaker constant (A_{131}). In this study, the cumulant mean diameter measured by DLS, corresponding to the Stokes diameter, was used as the effective particle diameter, d, and ψ_0 was approximated by the zeta potential.

The smectite particles used in this study are anisotropic platelets rather than spheres. Nevertheless, the sphere–sphere formulation was adopted as a common operational framework for comparing the four clay species under the same analytical conditions, using the DLS-derived diameter as a hydrodynamic effective diameter. In the non-retarded Hamaker approximation, the van der Waals interaction free energy per unit area between two idealized parallel planar surfaces scales as H^{-2}, whereas, for two equal spheres at surface separations small compared with the particle radius, the sphere–sphere interaction energy used here scales as H^{-1} [36]. The interaction magnitude for platelets also depends on their relative orientation and effective overlapping area. Therefore, replacing the spherical model with a platelet-based model would change the functional form and magnitude of

the calculated interaction potential and, consequently, the numerical values of $A_{H,app}$ and H^*. The direction and magnitude of these changes cannot be uniquely determined without information on particle orientation and effective interacting area. Accordingly, $A_{H,app}$ and H^* should be regarded as model-dependent effective parameters. In particular, H^* is an operational characteristic distance derived from the fitted slope and does not represent the exact physical gap between clay sheets.

For each sample, DLVO potential curves were calculated using the zeta potential and Debye length at the sol–gel transition boundary, and the height of the potential barrier, $(V/k_BT)_{max}$, was evaluated. Here, k_B is the Boltzmann constant and T is the absolute temperature. In DLVO theory, particle aggregation generally becomes more favorable as the potential barrier decreases, and rapid coagulation is known to occur when the barrier disappears [39]. Importantly, the sol–gel transition boundary itself was determined experimentally by rheological measurements and was not predicted from DLVO theory. The condition,

$$\left(\frac{V}{k_BT}\right)_{max} = 0, \tag{7}$$

was subsequently applied only as an operational mapping criterion for converting the experimentally observed boundary into a common DLVO-based parameter. Therefore, this condition should not be interpreted as a universal microscopic criterion for gelation or as implying that gelation is equivalent to primary-minimum coagulation. The Hamaker constant satisfying this condition was defined as the apparent Hamaker constant, $A_{H,app}$. It should be noted that this condition is not based on a rigorous theory of gelation, but is an analytical condition introduced to compare the sol–gel transition boundaries of different clay species using a common criterion. As a related approach, Leong and Ong (2003) [40] estimated the Hamaker constant for oxide particle dispersions by connecting the critical zeta potential at which the yield stress disappears with DLVO theory. Galli et al. (2020) [41] also proposed a method for determining the critical coagulation concentration (CCC) by evaluating the disappearance condition of the interparticle energy barrier from the zeta potential and DLVO theory. The derivation of $A_{H,app}$ in the present study can therefore be regarded as an operational method for converting experimentally observed transition boundaries into DLVO parameters, similarly to these previous studies. However, the present study extends this approach to the sol–gel transitions of aqueous smectite clay dispersions, with the aim of consistently comparing the transition boundaries among different clay species. The $A_{H,app}$ obtained in this study is not a true material constant but can be regarded as an effective parameter that includes the effects of particle shape, particle orientation, hydration, interlayer swelling, tactoid formation, and network structure formation.

3. Results and Discussion

3.1. Zeta Potential of Smectite Clay Dispersions

The zeta potentials of the clays in water were negative under all experimental conditions. In this paper, the zeta potential is therefore expressed as its absolute value in order to clarify the relationship between the absolute zeta potential, $|\zeta|$, and the NaCl concentration, [NaCl], as well as its effect on the DLVO potential curves. Under deionized, extremely low ionic-strength conditions, Gouy–Chapman theory [42,43] indicates that, when the surface charge density is constant, the surface potential increases approximately in proportion to the Debye length. Furthermore, assuming that the position of the slipping plane does not change significantly, the zeta potential in the low-salt-concentration region is also expected to show an approximately linear scaling with the inverse square root of the 1:1 electrolyte concentration, $1/\sqrt{c}$ [20,36].

The dependence of $|\zeta|$ on the inverse square root of the NaCl concentration, $1/\sqrt{[\mathrm{NaCl}]}$, was plotted for each clay in water (Figure 1). The solid, dashed, and dotted lines in Figure 1 represent linear fits to the data in the low-salt-concentration region at ϕ = 0.003, 0.002, and 0.001, respectively.

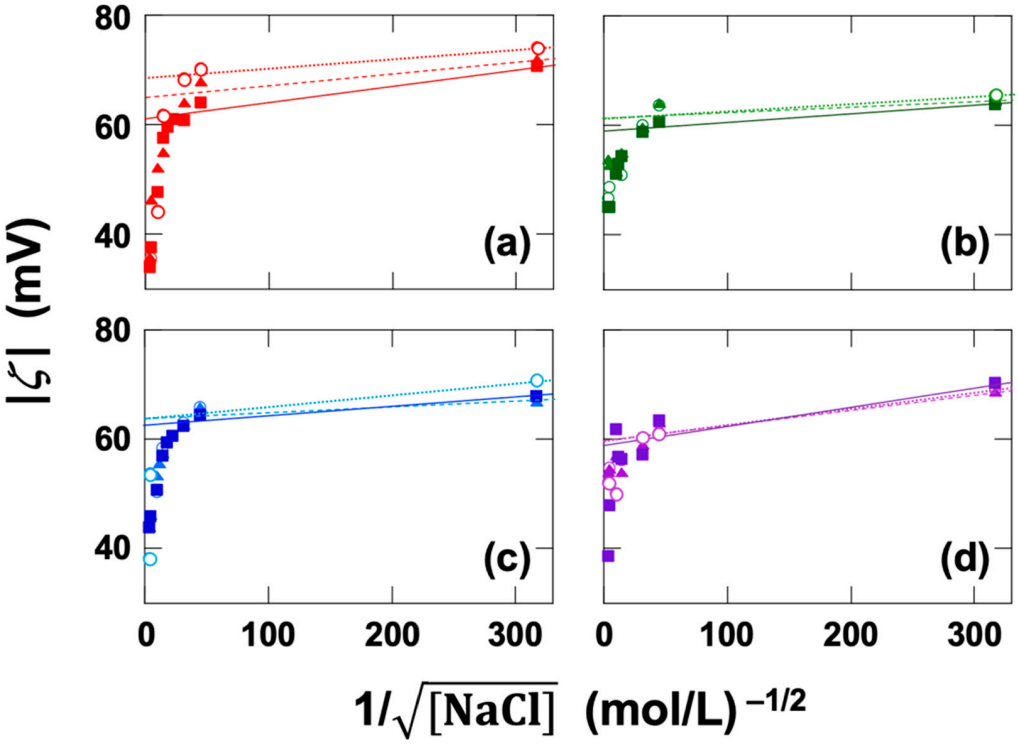


Figure 1. Dependence of the absolute value of the zeta potential, $|\zeta|$, on $1/\sqrt{[\mathrm{NaCl}]}$ for aqueous dispersions of four clays at 25 °C. (**a**) Fluorinated hectorite (Ht-F), (**b**) stevensite (Stv), (**c**) hectorite (Ht), and (**d**) saponite (Sap). Open circles: ϕ = 0.001, with the data in the low-salt-concentration region fitted by dotted lines; filled triangles: ϕ = 0.002, fitted by dashed lines; filled squares: ϕ = 0.003, fitted by solid lines. All symbols are color-coded according to clay species.

In the low-salt-concentration region ([NaCl] $\leq 10^{-3}$ mol/L), $|\zeta|$ showed an approximately linear relationship with $1/\sqrt{[\mathrm{NaCl}]}$ for all clays. For Ht-F, $|\zeta|$ tended to decrease with increasing ϕ, whereas this tendency was weak for Stv and Ht and was hardly observed for Sap. In contrast, in the high-salt-concentration region, $|\zeta|$ deviated from this linear relationship and decreased further with increasing [NaCl].

The linear relationship observed in the low-salt-concentration region can be explained by the screening effect of the electric double layer. In addition, the different ϕ dependences observed for Ht-F, Stv, Ht, and Sap suggest that, because the zeta potential mainly reflects the electric double-layer state near the particle surface, particularly near the slipping plane, differences in the magnitude and origin of the layer charge, exfoliation state, and hydration state of each clay may be reflected in the electric double-layer structure. On the other hand, in the region above approximately 10^{-3} mol/L, the Debye length becomes shorter, and contributions related to the electric double-layer structure near the particle surface, such as the Stern layer, strongly hydrated layers, specific adsorption of Na^+, and surface charge regulation, may become relatively more important [36,44]. Such salt-concentration dependence of the zeta potential in smectite clays has also been reported in many previous studies [25,45–47].

Table 1 shows $|\zeta|$ of the four clays in water in the high-salt-concentration region. All values listed in the table correspond to conditions near the sol–gel transition boundary and were used for the DLVO analysis. Measured values are shown in bold, whereas

interpolated values are shown in regular type. The interpolated values were obtained by linear interpolation with respect to the common logarithm of the NaCl concentration using the neighboring measured values.

Table 1. Absolute values of the zeta potentials, $|\zeta|$, of clays in water used to construct the DLVO potential curves at 25 °C. Measured values are shown in bold, and interpolated values are shown in regular font. The values of $1/\sqrt{[\mathrm{NaCl}]}$ are also shown; a dash (–) indicates a condition that was not included in the DLVO analysis.

		[NaCl] (mol/L)							
Clay	φ	0.005	0.007	0.008	0.01	0.03	0.05	0.07	0.1
$(1/\sqrt{([\mathrm{NaCl}])}\ \mathrm{L}^{1/2}\mathrm{mol}^{-1/2})$		(14.1)	(12.0)	(11.2)	(10.0)	(5.77)	(4.47)	(3.78)	(3.16)
Ht-F									
	0.001	**–**	**–**	**–**	**–**	**–**	**35.59**	35.27	**34.93**
	0.002	**55.00**	53.62	–	**52.17**	–	**46.27**	41.19	**35.82**
	0.003	**57.63**	52.86	–	**47.80**	–	–	–	–
Stv									
	0.001	–	–	–	–	–	**48.82**	47.82	**46.77**
	0.002	–	53.29	52.65	**51.58**	–	**52.74**	53.30	**53.89**
	0.003	–	52.94	52.29	**51.20**	–	–	–	–
Ht									
	0.001	–	55.69	53.00	**50.40**	52.76	**53.85**	46.28	**38.25**
	0.002	**57.41**	**55.69**	54.80	**53.30**	48.47	**46.23**	45.06	**43.82**
	0.003	**57.06**	–	–	–	–	–	–	–
Sap									
	0.001	–	–	–	–	–	–	–	**52.16**
	0.002	–	–	–	**57.08**	55.34	**54.54**	–	**54.04**
	0.003	–	–	–	**61.83**	52.35	**47.94**	–	–

3.2. Sol–Gel State Diagram

In this study, the frequency dependence of the storage modulus, G', and loss modulus, G'', near the sol–gel transition was examined to construct sol–gel state diagrams (Figure 2). In Figure 2a (Ht-F: ϕ = 0.003, [NaCl] = 0.003 mol/L), G'' is higher than G', whereas in Figure 2b (Ht: ϕ = 0.002, [NaCl] = 0.007 mol/L), G' is higher than G''. For both samples, the frequency dependence of G' and G'' was small within the measurement range. In addition, G' tended to increase with increasing ϕ and [NaCl].

Winter and Chambon (1986) [48] reported critical gel behavior in chemically crosslinked polymers, in which G' and G'' follow the same power law at the gel point. The weak frequency dependence observed in the present study should not be interpreted as such Winter–Chambon-type critical gel behavior, but rather as colloidal-gel-like viscoelastic behavior originating from interparticle interactions. On the other hand, changes in the relative magnitudes of G' and G'' with varying ϕ and [NaCl] have been widely reported for colloidal gels and clay gels possessing spatial network structures formed by interparticle interactions [32,49–51]. These results suggest that, near the sol–gel transition boundary, the present system behaves as a colloidal physical gel in which a network structure is formed by interparticle interactions and develops with gelation.

Sol–gel state diagrams were constructed based on the results of the dynamic viscoelastic measurements (Figure 3).

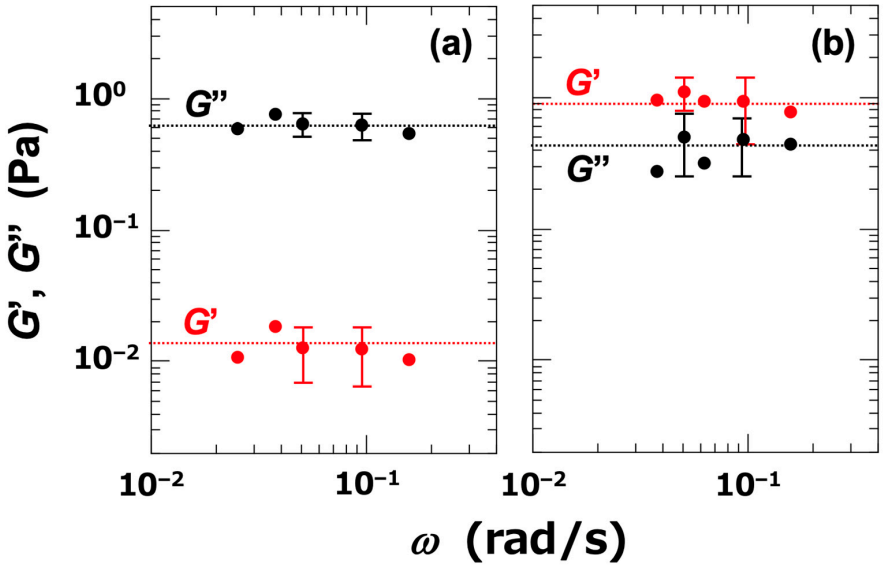


Figure 2. Examples of the angular frequency dependence of the storage modulus, G', and loss modulus, G'', for aqueous clay dispersions near the sol–gel transition boundary at 25 °C. The applied shear strain was $\gamma = 0.002$. (**a**) Ht-F, $\phi = 0.003$, [NaCl] = 0.003 mol/L, tan $\delta > 1$ (sol state); (**b**) Ht, $\phi = 0.002$, [NaCl] = 0.007 mol/L, tan $\delta < 1$ (gel state). Error bars indicate the ranges between the minimum and maximum values of G' and G'' observed during the measurements.

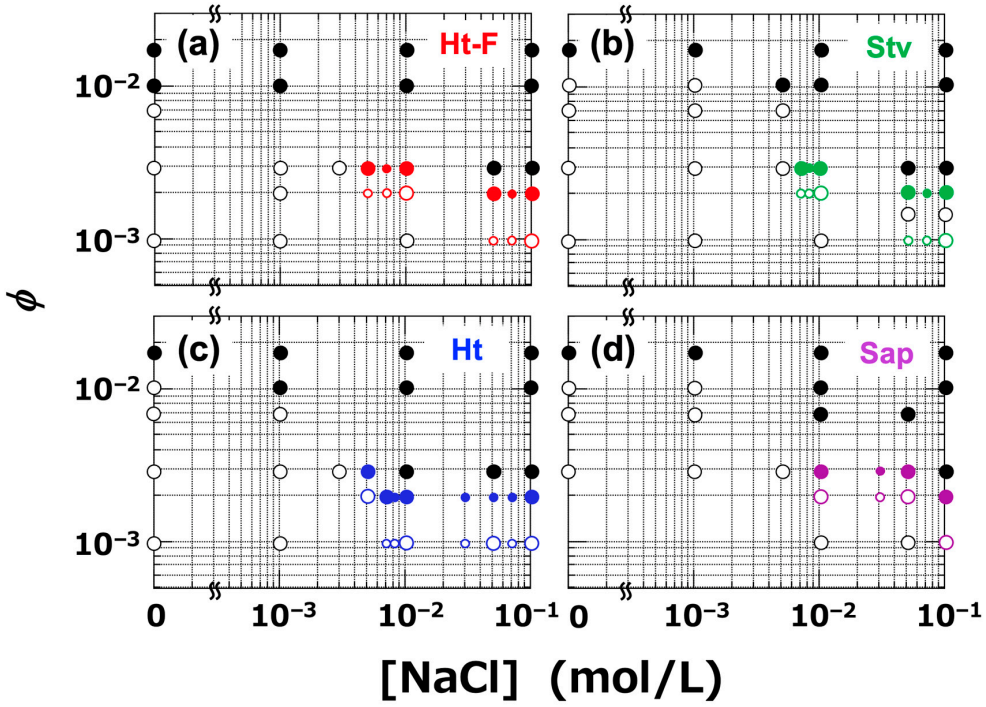


Figure 3. Sol–gel state diagrams of aqueous dispersions of four clays at 25 °C. (**a**) Ht-F, (**b**) Stv, (**c**) Ht, and (**d**) Sap. The sol–gel state was determined by dynamic rheological measurements. The applied shear strain was $\gamma = 0.002$, and the angular frequency was $\omega = 0.05$ rad/s. Open circles: sol state (tan $\delta > 1$); filled circles: gel state (tan $\delta < 1$). Colored symbols indicate the experimental conditions near the sol–gel transition boundary used for DLVO analysis. Large symbols represent states determined from experimental results, whereas small symbols represent states estimated by interpolation from surrounding measurement results. The colors distinguish the four clay species and are used consistently in the subsequent figures. Grid lines are included to facilitate identification of the experimental conditions; except for $\phi = 0.017$, all plotted data points are located at grid-line intersections.

Open and filled circles represent the sol and gel states, respectively, and colored symbols indicate the data used for the DLVO analysis. For all clays, gelation was promoted by increasing the clay concentration and NaCl concentration. However, the clay and NaCl concentrations at which the sol–gel transition occurred differed depending on the clay species. This result indicates that, even within the same family of smectite clays, the ease of gel-network formation differs markedly among clay species. The rheologically determined sol–gel regions are also consistent with our previously reported sessile-droplet drying-pattern observations [26], in which ring-shaped deposits were observed predominantly in the sol region, bump-shaped deposits in the gel region, and coexistence of ring- and bump-type patterns near the sol–gel boundary. This independent correspondence provides additional experimental support for the identification of the sol–gel boundary used in the present analysis. The authors have previously reported clear clay-species dependence in the transparency and rheological properties of deionized gels [24,25]. The sol–gel state diagrams obtained in this study indicate that these differences in physical properties are closely related to differences in gel-network-forming ability. On the other hand, the zeta potential alone cannot sufficiently explain the distance scale over which such differences in network-forming ability emerge. Therefore, in this study, a distance parameter governing the clay-species dependence is examined by DLVO analysis using the sol–gel transition boundary.

3.3. Apparent Hamaker Constant Derived from DLVO Analysis

Smectite clays are platelet-like particles, and their surface charge distribution is not uniform; therefore, interparticle interactions strongly depend on particle orientation. Permanent negative charges originating from isomorphic substitution in the crystal lattice are mainly distributed on the basal faces, whereas Al–OH and Si–OH groups are present at the edge sites. Thus, various interaction modes, such as face–face (FF), edge–edge (EE), and edge–face (EF) interactions, are known to occur between clay particles. On the other hand, all dispersions used in this study were under mildly alkaline conditions (pH = 7.6–8.9), and both the basal faces and edge sites are considered to be negatively charged on average [24]. Under these conditions, strongly attractive electrostatic edge–face interactions are therefore not expected to dominate. However, because particle orientations were not directly determined in the present study, the DLVO analysis should not be assigned to a specific geometrical configuration. Instead, the present DLVO analysis provides a simplified, effective description of the competition between electric double-layer repulsion and van der Waals attraction, without assigning the interaction to a specific particle orientation.

For each sample, DLVO potential curves were calculated using the zeta potential and Debye length at the sol–gel transition boundary (Figure 4).

In this study, the condition $(V/k_BT)_{max} = 0$ was applied as an operational mapping criterion to the experimentally determined sol–gel transition boundary, and the Hamaker constant satisfying this condition was defined as the apparent Hamaker constant, $A_{H,app}$. In Figure 4, the DLVO potential curves corresponding to $A_{H,app}$ are shown as red solid lines, while potential curves calculated by assuming nearby Hamaker constant values are also shown as black solid lines for comparison. For all clays, $A_{H,app}$ decreased with increasing NaCl concentration (Table 2).

This behavior is clearly different from that of the true Hamaker constant. In general, van der Waals attraction is an intrinsic material interaction determined by the dielectric properties of the particles and the dispersion medium and is evaluated based on Lifshitz theory [52]. Therefore, the Hamaker constant usually does not vary markedly with electrolyte concentration [36,53–55]. Calculations based on Lifshitz theory have reported a Hamaker constant of approximately 5×10^{-21} J for montmorillonite [56]. Hamaker constants for inor-

ganic particles in water are generally on the order of 10^{-20}–10^{-19} J, and similar values have also been used in DLVO analyses of clay minerals [21,36,54,57]. However, the $A_{H,app}$ values obtained in this study showed a clear salt-concentration dependence and varied over a wide range of 10^{-20}–10^{-19} J. This result suggests that $A_{H,app}$ is not the true Hamaker constant itself, but rather a composite effective parameter that maps the experimentally observed sol–gel boundary onto the simplified DLVO framework. Particularly in the low-salt region, $A_{H,app}$ may effectively incorporate not only van der Waals attraction but also the influence of long-range electrostatic repulsion, hydration and other non-DLVO interactions, particle orientation, tactoid formation, and collective constraints or spatial jamming associated with network formation or arrested states [58–60]. This interpretation is also consistent with molecular dynamics simulation results showing that non-DLVO interactions arising from hydration structures and ion correlations play important roles in smectite interparticle interactions [59,60]. Furthermore, Gao et al. (2022) [21] reported an effective Hamaker constant of approximately 1.1×10^{-19} J from critical coagulation concentration analysis of montmorillonite dispersions, which is of the same order as the $A_{H,app}$ values obtained in this study. This supports the interpretation that $A_{H,app}$ introduced in this study is not an unrealistic quantity, but rather an effective parameter reflecting the aggregation and gelation behavior of clay dispersions.

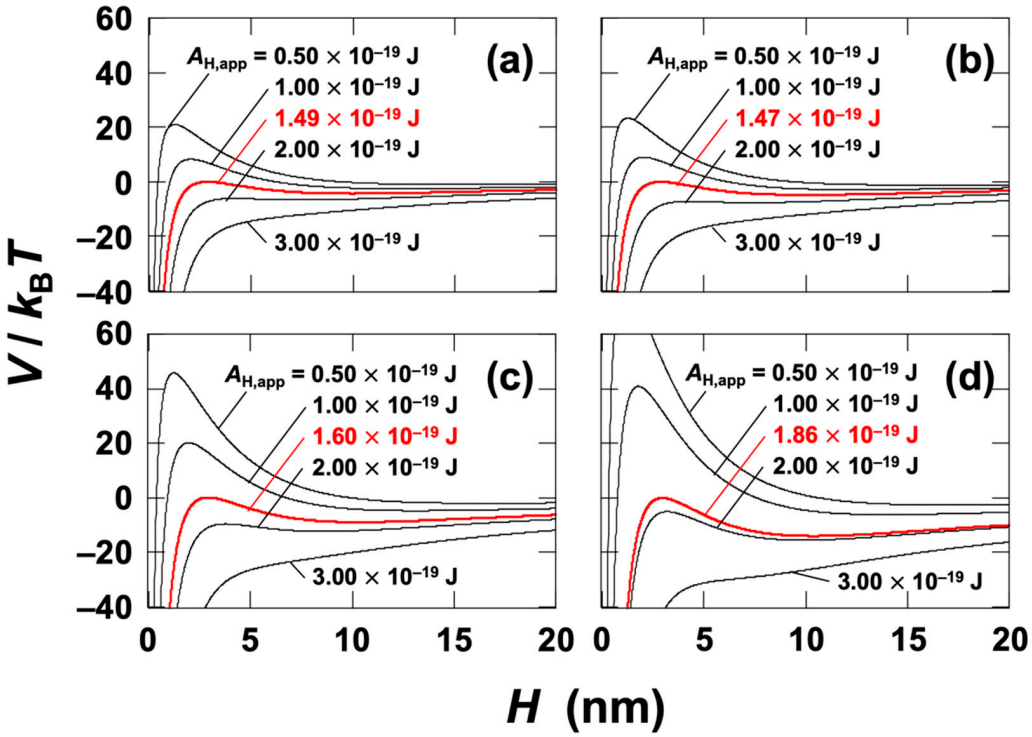


Figure 4. Examples of DLVO potential curves for four clays in water at 25 °C. (**a**) Ht-F, d = 40 nm, $|\zeta|$ = 52.2 mV, L_D = 3.04 nm; (**b**) Stv, d = 46 nm, $|\zeta|$ = 51.6 mV, L_D = 3.04 nm; (**c**) Ht, d = 79 nm, $|\zeta|$ = 53.3 mV, L_D = 3.04 nm; and (**d**) Sap, d = 108 nm, $|\zeta|$ = 57.1 mV, L_D = 3.04 nm. ϕ = 0.002 and [NaCl] = 0.01 mol/L. The red curves represent the DLVO potential curves calculated using the apparent Hamaker constant, $A_{H,app}$, determined under each condition.

What is important in this study is not the absolute value of $A_{H,app}$ itself, but rather the fact that a distance scale characterizing network formation can be extracted from its electrolyte concentration dependence. Accordingly, the electrolyte concentration dependence of $A_{H,app}$ was analyzed to derive a distance parameter, H^*, that characterizes network formation.

Table 2. Apparent Hamaker constants, $A_{H,app}$ (10^{-19} J), obtained by DLVO analysis at 25 °C. Values calculated using measured zeta potentials are shown in bold, whereas those calculated using interpolated zeta potentials are shown in regular font. The values of $1/L_D$ are also shown together with the NaCl concentrations. A dash (–) indicates a condition that was not included in the calculation of $A_{H,app}$.

		[NaCl] (mol/L)							
Clay	φ	0.005	0.007	0.008	0.01	0.03	0.05	0.07	0.1
($1/L_D$ nm^{-1})		(0.23)	(0.27)	(0.30)	(0.33)	(0.57)	(0.73)	(0.87)	(1.04)
Ht-F									
	0.001	–	–	–	–	–	**0.321**	0.268	**0.221**
	0.002	**2.27**	1.85	–	**1.49**	–	**0.543**	0.366	**0.232**
	0.003	**2.50**	1.80	–	**1.25**	–	–	–	–
Stv									
	0.001	–	–	–	–	–	**0.607**	0.495	**0.397**
	0.002	–	1.85	1.70	**1.47**	–	**0.709**	0.615	**0.527**
	0.003	–	1.82	1.68	**1.45**	–	–	–	–
Ht									
	0.001	–	2.08	1.77	**1.44**	0.924	**0.747**	0.468	**0.268**
	0.002	**2.59**	**2.08**	1.90	**1.60**	0.780	**0.551**	0.444	**0.351**
	0.003	**2.56**	–	–	–	–	–	–	–
Sap									
	0.001	–	–	–	–	–	–	–	**0.499**
	0.002	–	–	–	**1.86**	1.020	**0.770**	–	**0.536**
	0.003	–	–	–	**2.18**	0.915	**0.595**	–	–

*3.4. Characteristic Interaction Distance H**

To clarify the electrolyte concentration dependence of $A_{H,app}$, the relationship between $\ln(A_{H,app}/10^{-20}$ J) and the reciprocal Debye length, $1/L_D$, was examined (Figure 5).

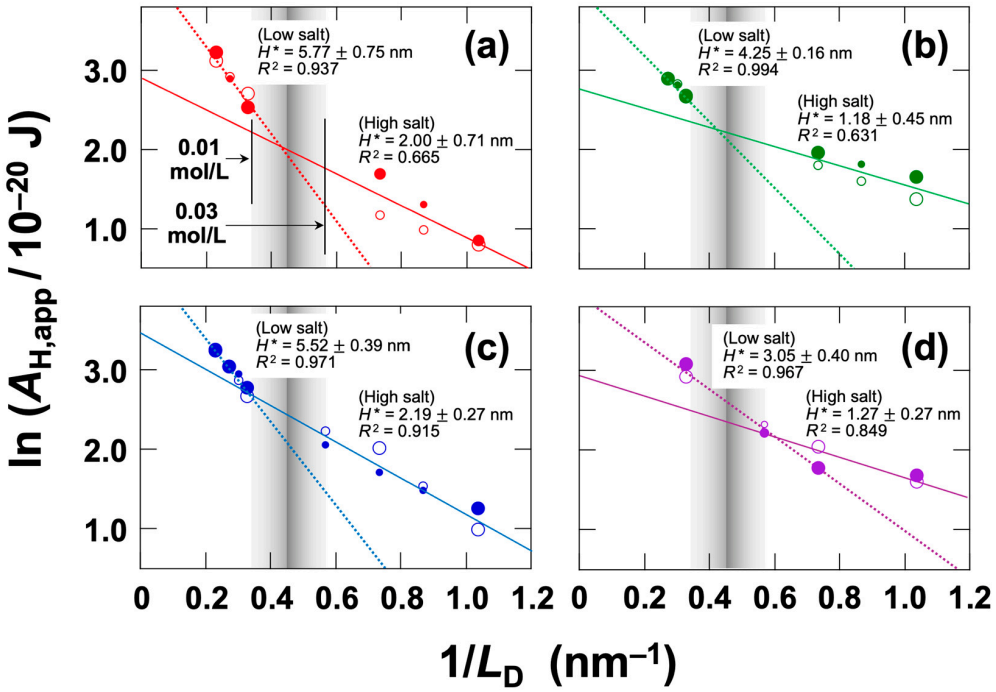


Figure 5. Dependence of the apparent Hamaker constant, $A_{H,app}$, on $1/L_D$ at 25 °C. (**a**) Ht-F, (**b**) Stv, (**c**) Ht, and (**d**) Sap. The vertical axis is expressed as $\ln(A_{H,app}/10^{-20}$ J). The symbols correspond to

the conditions indicated in Figure 3: open symbols represent sol states and filled symbols represent gel states. Symbol size follows the notation used in Figure 3. Linear fits were performed separately using the data at [NaCl] $\leq$ 0.01 mol/L for the low-salt region and at [NaCl] $\geq$ 0.03 mol/L for the high-salt region. For Sap, however, only one NaCl concentration (0.01 mol/L) was available within the low-salt range; therefore, the data at 0.01 and 0.03 mol/L were used to estimate the lower-salt-side slope. Accordingly, for Sap only, the 0.03 mol/L data were included in both fits as points at the boundary between the two regimes. The interval between 0.01 and 0.03 mol/L is indicated as the crossover region. The symbols and fitted lines in panels (**a**–**d**) are color-coded consistently with Figure 3. The H^* values shown in each panel were determined from the negative slopes of the linear fits and are presented as estimates $\pm$ 1 standard error; the corresponding coefficients of determination (R^2) are also indicated. The stated uncertainties represent only the statistical uncertainty associated with the linear fits and do not include systematic or experimental uncertainties arising from the measurements or data interpolation.

As a result, approximately linear relationships were observed between these quantities for all clays, although the goodness of fit varied depending on the clay species and salt-concentration region. The R^2 values ranged from 0.937 to 0.994 in the low-salt region and from 0.631 to 0.915 in the high-salt region. This result is consistent with the exponential decay of electric double-layer repulsion with the surface-to-surface separation, expressed as $\exp(-H/L_D)$, and suggests that $A_{H,app}$ at the sol–gel transition boundary exhibits an $\exp(-H^*/L_D)$-type dependence.

The linear relationship in each region was expressed by the following equation:

$$\ln(A_{H,app}/10^{-20}\mathrm{J}) = \ln(A_{H,0}/10^{-20}\mathrm{J}) - \frac{H^*}{L_D}. \quad (8)$$

Here, $A_{H,0}$ is the formally extrapolated value of $A_{H,app}$ at $1/L_D = 0$, corresponding to the intercept of the linear fit, and H^* is the characteristic interaction distance determined from the negative slope of the linear fit. The uncertainty in H^* was evaluated from the standard error of the fitted slope. The uncertainty in $A_{H,0}$ was obtained by transforming the fitted intercept and its $\pm$1 standard-error limits through the exponential relation used to calculate $A_{H,0}$. It should be noted that H^* does not represent the actual surface-to-surface separation, H, in DLVO theory, but is an effective structural parameter derived from the sol–gel transition boundary. Because the lower-salt-side fit for Sap was based on only two NaCl concentration levels (0.01 and 0.03 mol/L), its H^* estimate and R^2 should be interpreted more cautiously than those for the other three clays. In particular, this fit does not establish linearity over a wider low-salt concentration range.

The data were approximated by lower- and higher-salt linear trends for all four clays, subject to the above limitation of the lower-salt-side fit for Sap. The change between these trends occurred within the experimentally resolved concentration interval of approximately 0.01–0.03 mol/L. This interval is referred to here as the crossover region; it should not be interpreted as a statistically optimized single breakpoint. Furthermore, this crossover appeared in nearly the same salt-concentration range for all four clays. These results suggest that the network-forming state associated with the sol–gel transition may change with salt concentration.

The relationship between H^* and $A_{H,0}$, determined from the linear fits in Figure 5, is shown in Figure 6.

For all clays, $A_{H,0}$ tended to increase with increasing H^*. However, because H^* and $A_{H,0}$ are derived from the slope and intercept, respectively, of the same linear regression, they are not statistically independent, and part of their apparent correlation may arise mathematically from the fitting procedure itself. Therefore, Figure 6 should be regarded primarily as a visualization of the systematic changes in the fitted parameters between

the lower- and higher-salt regimes, rather than as evidence of an independent physical relationship between H^* and $A_{H,0}$.

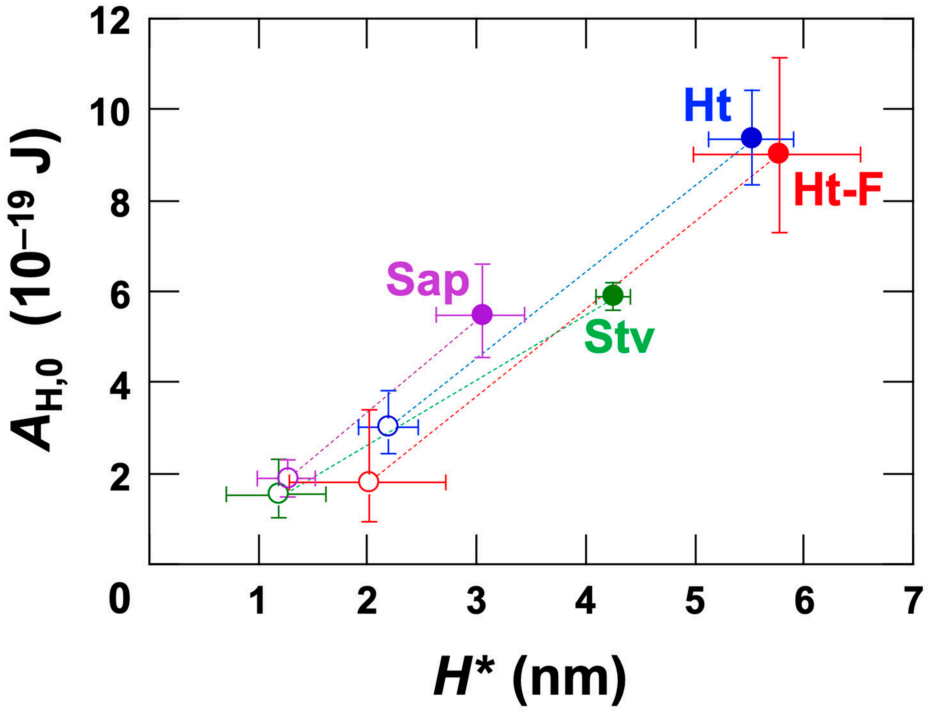


Figure 6. Relationship between the apparent Hamaker constant $A_{H,0}$ and the characteristic interaction distance H^* for four clays at 25 °C. H^* was determined from the negative slope of each linear fit in Figure 5, whereas $A_{H,0}$ was calculated from the corresponding fitted intercept, $\ln(A_{H,0}/10^{-20}$ J). Filled symbols represent values obtained from the low-salt-concentration fits, whereas open symbols represent those obtained from the high-salt-concentration fits. The colors identify the clay species consistently with Figures 3 and 5. Dashed lines connect the low- and high-salt values for the same clay species. Horizontal error bars represent the standard errors of H^* derived from the fitted slopes. Vertical error bars represent the uncertainty in $A_{H,0}$ calculated from the standard error of the fitted intercept. These error bars represent only the statistical uncertainty associated with the linear fits; systematic and experimental uncertainties arising from the measurements and data interpolation were not propagated.

In the low-salt-concentration region, the point estimates of H^* followed the order Ht-F > Ht > Stv > Sap. However, this ordering should be regarded as descriptive because no formal pairwise comparison of the fitted slopes was performed, and some estimates, particularly those for Ht-F and Ht, overlapped within their fitting uncertainties. The H^* values ranged from 3.05 to 5.77 nm on the lower-salt side, whereas they decreased to 1.18–2.19 nm on the higher-salt side. In the high-salt-concentration region, several clay-species estimates overlapped within their fitting uncertainties, indicating that the clay-species dependence became less clearly differentiated. Thus, the principal result is the decrease in H^* from the lower- to the higher-salt regime for each clay, rather than an exact statistically established ranking among the four clays. In the lower-salt regime, the longer-range electrostatic repulsion is consistent with a relatively fine network formed by more spatially separated clay units. With increasing NaCl concentration, compression of the electric double layer permits closer particle approach, which may promote network coarsening and local stacking or tactoid formation. Analysis of the characteristic interaction distance, H^*, suggested a change in the network-forming state within the experimentally resolved range of approximately 0.01–0.03 mol/L for all clays. To examine whether this crossover was associated with

changes in network structure, the NaCl concentration dependence of transmittance was investigated (Figure 7).

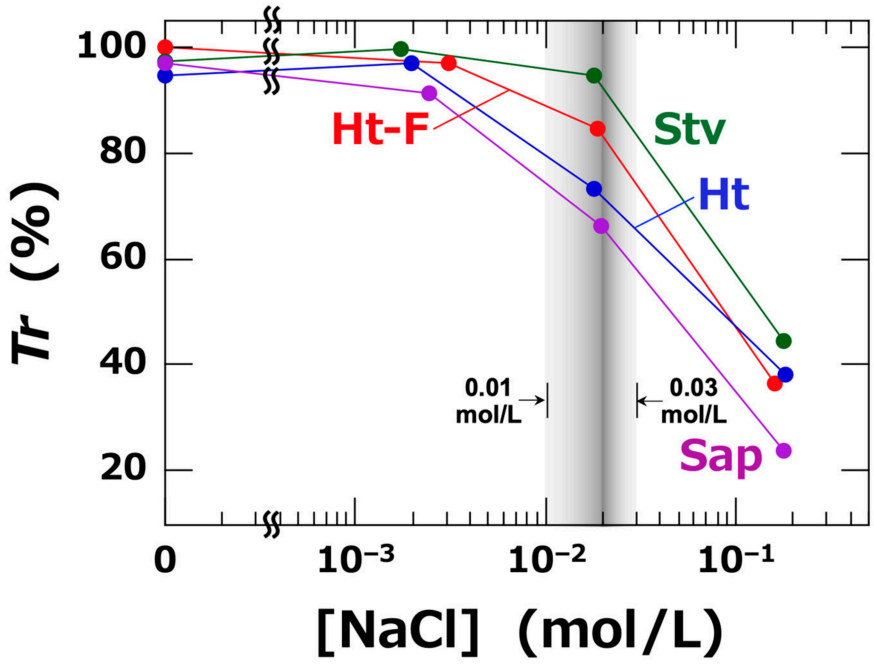


Figure 7. Effect of NaCl concentration on the transmittance, *Tr*, of aqueous dispersions of four clays at 25 °C. The clay volume fraction was ϕ = 0.003. Filled circles show the experimental data, and the colors distinguish the clay species: red, fluorinated hectorite (Ht-F); green, stevensite (Stv); blue, hectorite (Ht); and purple, saponite (Sap).

All dispersions showed relatively high transmittance in the low-salt-concentration region; however, the transmittance decreased with increasing NaCl concentration. In particular, the decrease in transmittance became pronounced above approximately 0.01 mol/L. This NaCl concentration range roughly coincided with the concentration range where H^* exhibited a crossover, approximately 0.01–0.03 mol/L.

Previous microstructural observations [24] showed relatively fine network structures at low salt concentrations and pronounced coarsening of the network framework at higher salt concentrations, with the structural change becoming evident around approximately 0.01 mol/L. These observations are consistent with the interpretation that compression of the electric double layer promotes closer particle approach and network coarsening. However, the present results do not directly demonstrate nanoscale tactoid formation. Such structural changes are also consistent with the observed decrease in transmittance with increasing NaCl concentration. In addition, at a higher clay volume fraction (ϕ = 0.01), the order of transmittance in the low-salt-concentration region was Ht-F > Ht ≈ Stv > Sap, which was broadly consistent with the clay-species trend in the low-salt H^* point estimates. Furthermore, the magnitude of the transmittance decrease with increasing NaCl concentration followed the order Ht-F > Ht > Stv > Sap, which was broadly consistent with the descriptive ordering of the low-salt H^* point estimates. These correspondences are consistent with the interpretation that H^* captures an effective distance scale associated with changes in the network-forming state; however, H^* should not be interpreted as a directly measured microscopic separation distance.

Furthermore, the authors have previously reported the NaCl concentration dependence of the yield stress, storage modulus, and loss modulus for aqueous dispersions of four smectite clays [25]. In that study, these values were found to increase on the high-salt-concentration side beyond the crossover region, regardless of clay species. These

rheological features are also consistent with the interpretation in the present study that the network-forming state changes with increasing NaCl concentration.

It should be emphasized, however, that this comparison involves datasets acquired at non-identical clay volume fractions. H^* was derived from conditions along the sol–gel boundaries, for which ϕ varied with clay species and NaCl concentration, whereas the transmittance data in Figure 7 were obtained at a fixed ϕ = 0.003, and the previously reported rheological data were obtained at the volume fractions specified in ref. [25]. Because the network-forming state depends on both ϕ and [NaCl], the agreement in the range of approximately 0.01–0.03 mol/L should be regarded as a qualitative correspondence between broad concentration regimes, rather than as a point-by-point correlation or evidence of a volume-fraction-independent transition concentration.

*3.5. Physical Meaning of H**

The characteristic interaction distance, H^*, defined in this study, is not the actual surface-to-surface separation, H, in DLVO theory, but an effective distance parameter derived from the sol–gel transition boundary. In actual smectite dispersions, interparticle interactions are known to be affected by various factors, including particle orientation, hydration, tactoid formation, and non-DLVO interactions [23,44,59–61]. Therefore, H^* should not be regarded as the actual distance between particle surfaces, but rather as an effective structural length scale for network formation that reflects the averaged effects of these multiple factors.

In this study, the clay-species trend in the point estimates of H^* in the low-salt-concentration region was broadly consistent with the clay-species dependence of transmittance reported in a previous study. In addition, within the limitations arising from the non-identical clay volume fractions described above, the H^* crossover observed at approximately 0.01–0.03 mol/L showed a qualitative correspondence with the decrease in transmittance observed in this study and with previously reported changes in yield stress, storage modulus, and loss modulus. These qualitative correspondences are consistent with the interpretation that H^* is an effective structural parameter associated with changes in the network-forming state.

On the other hand, the clay-species dependence of H^* did not simply correspond to any single material property, such as particle size or CEC. For example, although Ht-F and Sap have nearly the same CEC, their H^* values differed markedly. Sap has layer charges originating from tetrahedral substitution [62,63], and thus the origin of its layer charge differs from that of the other clays. Such differences in the origin of layer charge have been suggested to affect not only the electric double-layer structure near the particle surface but also tactoid formation and the exfoliation state through interparticle interactions [62–64]. Therefore, these differences may also be involved in the characteristic H^* behavior observed for Sap. These considerations suggest that H^* may reflect the combined influence of multiple factors associated with network formation, including particle size, particle orientation, tactoid formation, non-DLVO interactions, and network structure, as well as near-surface properties such as layer charge, exfoliation state, and hydration state. Based on these results, H^* can be interpreted as an effective structural parameter associated with the network-forming state of clay dispersions. Whereas the zeta potential mainly reflects the strength of electrostatic repulsion near the particle surface, H^* provides an effective distance scale associated with how such interactions manifest in network formation. Therefore, H^* can be considered a parameter that provides information complementary to the zeta potential for understanding the sol–gel transitions of aqueous smectite clay dispersions.

4. Conclusions

In this study, sol–gel state diagrams were constructed over a wide range of clay and NaCl concentrations for aqueous dispersions of four smectite clays: fluorinated hectorite (Ht-F), stevensite (Stv), hectorite (Ht), and saponite (Sap). Based on DLVO analysis, the apparent Hamaker constant, $A_{H,app}$, was calculated from the experimentally determined sol–gel transition boundaries. The resulting $A_{H,app}$ should be regarded as an effective parameter rather than a true material constant. Approximately linear relationships were observed between $\ln(A_{H,app}/10^{-20}\ \mathrm{J})$ and the reciprocal Debye length, $1/L_D$, for all clays, with distinct trends in the low- and high-salt-concentration regions. A crossover between these trends was observed at approximately 0.01–0.03 mol/L NaCl. This concentration range roughly coincided with the range in which the transmittance obtained in this study began to decrease and was also consistent with the salt-concentration dependence of yield stress, storage modulus, and loss modulus reported in the authors' previous study. However, because the transmittance and previously reported rheological datasets were acquired at non-identical clay volume fractions, this correspondence should be regarded as qualitative and does not establish a volume-fraction-independent transition concentration.

In this study, the distance scale derived from the negative slope of the linear relationship between $\ln(A_{H,app}/10^{-20}\ \mathrm{J})$ and $1/L_D$ was defined as the characteristic interaction distance, H^*. H^* is not the actual surface-to-surface separation in DLVO theory but can be interpreted as an effective structural parameter that may reflect the combined influence of multiple factors associated with network formation, including particle orientation, tactoid formation, non-DLVO interactions, and network structure, as well as near-surface properties that also affect the zeta potential.

H^* showed greater variation among clay species in the low-salt-concentration region, whereas it became smaller and less clearly differentiated among clay species in the high-salt-concentration region. Because no formal pairwise comparison of the fitted slopes was performed and some estimates overlapped within their fitting uncertainties, the exact interspecies ordering should be regarded as descriptive. The clay-species trend in the low-salt-concentration region was broadly consistent with the previously reported transmittance behavior.

Based on these results, the zeta potential can be regarded as an indicator that mainly reflects the strength of electrostatic repulsion associated with the electric double-layer state near the particle surface. In contrast, H^* provides an effective distance scale associated with how such interactions manifest in network formation. In addition, within the limitations arising from the non-identical clay volume fractions, the crossover observed at approximately 0.01–0.03 mol/L showed a qualitative correspondence with changes in transmittance and previously reported rheological properties, consistent with the interpretation that the network-forming state changes across this concentration range.

The analysis based on the apparent Hamaker constant and the characteristic interaction distance, H^*, proposed in this study provides a useful framework for interpreting the sol–gel transition, network formation, optical properties, and rheological properties of aqueous smectite clay dispersions from the complementary viewpoints of interaction strength and effective distance scale. Furthermore, this approach may be applicable to comparative analyses of network formation in other anisotropic colloidal dispersions and physical gel systems, provided that an experimentally defined transition boundary and an appropriate interaction model are available.

A more rigorous description incorporating platelet geometry, particle orientation, orientation-dependent interactions, and tactoid formation will be an important subject for future development of this analytical framework.

Author Contributions: Conceptualization, H.K.; methodology, H.K.; validation, H.K.; investigation, H.K., H.T. and S.S.; resources, H.K., H.T. and S.S.; data curation, H.K.; writing—original draft preparation, H.K.; writing—review and editing, H.K., H.T. and S.S.; visualization, H.K.; supervision, H.K.; project administration, H.K. All authors have read and agreed to the published version of the manuscript.

Funding: This research received no specific grant from any funding agency in the public, commercial, or nonprofit sectors.

Institutional Review Board Statement: Not applicable.

Informed Consent Statement: Not applicable.

Data Availability Statement: The data presented in this study are contained within the article.

Acknowledgments: The authors are grateful to T. Numata, K. Shibata, T. Shimomaki, and S. Ikeno for their support in conducting the experiments. This research was supported in part by the use of facilities at the Division of Instrumental Analysis, Life Science Research Center, Gifu University.

Conflicts of Interest: H.K. has a collaborative research relationship with KUNIMINE INDUSTRIES Co., Ltd. H.T. and S.S. are employees of KUNIMINE INDUSTRIES Co., Ltd. The experiments and main analyses reported in this manuscript were conducted and largely completed before the start of the collaborative research project. The authors declare no other conflicts of interest.

References

1. van Olphen, H. *An Introduction to Clay Colloid Chemistry: For Clay Technologists, Geologists, and Soil Scientists*, 2nd ed.; Wiley: New York, NY, USA, 1977.
2. Bergaya, F.; Lagaly, G. General introduction: Clays, clay minerals, and clay science. In *Handbook of Clay Science*, 2nd ed.; Bergaya, F., Lagaly, G., Eds.; Elsevier: Amsterdam, The Netherlands, 2013; pp. 1–19.
3. Mourchid, A.; Lécolier, E.; Van Damme, H.; Levitz, P. On viscoelastic, birefringent, and swelling properties of Laponite clay suspensions: Revisited phase diagram. *Langmuir* **1998**, *14*, 4718–4723. [CrossRef]
4. Levitz, P.; Lécolier, E.; Mourchid, A.; Delville, A.; Lyonnard, S. Liquid–solid transition of Laponite suspensions at very low ionic strength: Long-range electrostatic stabilization of anisotropic colloids. *Europhys. Lett.* **2000**, *49*, 672–677. [CrossRef]
5. Ruzicka, B.; Zaccarelli, E.; Zulian, L.; Angelini, R.; Sztucki, M.; Moussaïd, A.; Narayanan, T.; Sciortino, F. Observation of empty liquids and equilibrium gels in a colloidal clay. *Nat. Mater.* **2011**, *10*, 56–60. [CrossRef]
6. Forbes, E.; Chryss, A. Fundamentals of clays surface and colloid science, and rheology. In *Clays in the Minerals Processing Value Chain*; Gräfe, M., Klauber, C., McFarlane, A.J., Robinson, D.J., Eds.; Cambridge University Press: Cambridge, UK, 2017; pp. 81–110.
7. Luckham, P.F.; Rossi, S. The colloidal and rheological properties of bentonite suspensions. *Adv. Colloid Interface Sci.* **1999**, *82*, 43–92. [CrossRef]
8. Lagaly, G. Colloid clay science. In *Handbook of Clay Science*; Bergaya, F., Theng, B.K.G., Lagaly, G., Eds.; Elsevier: Amsterdam, The Netherlands, 2006; Volume 1, pp. 141–245.
9. Brunchi, C.-E.; Morariu, S. Laponite®—From dispersion to gel—Structure, properties, and applications. *Molecules* **2024**, *29*, 2823. [CrossRef]
10. Mourchid, A.; Delville, A.; Lambard, J.; Lécolier, E.; Levitz, P. Phase diagram of colloidal dispersions of anisotropic charged particles: Equilibrium properties, structure, and rheology of Laponite suspensions. *Langmuir* **1995**, *11*, 1942–1950. [CrossRef]
11. Kroon, M.; Vos, W.L.; Wegdam, G.H. Structure and formation of a gel of colloidal disks. *Phys. Rev. E* **1998**, *57*, 1962–1970. [CrossRef]
12. Mongondry, P.; Tassin, J.-F.; Nicolai, T. Revised state diagram of Laponite dispersions. *J. Colloid Interface Sci.* **2005**, *283*, 397–405. [CrossRef]
13. Dijkstra, M.; Hansen, J.P.; Madden, P.A. Gelation of a clay colloid suspension. *Phys. Rev. Lett.* **1995**, *75*, 2236–2239. [CrossRef]
14. Dijkstra, M.; Hansen, J.P.; Madden, P.A. Statistical model for the structure and gelation of smectite clay suspensions. *Phys. Rev. E* **1997**, *55*, 3044–3053. [CrossRef]
15. Ruzicka, B.; Zulian, L.; Ruocco, G. Routes to gelation in a clay suspension. *Phys. Rev. Lett.* **2004**, *93*, 258301. [CrossRef]
16. Ruzicka, B.; Zulian, L.; Ruocco, G. More on the phase diagram of Laponite. *Langmuir* **2006**, *22*, 1106–1111. [CrossRef]
17. Lagaly, G.; Ziesmer, S. Colloid chemistry of clay minerals: The coagulation of montmorillonite dispersions. *Adv. Colloid Interface Sci.* **2003**, *100–102*, 105–128. [CrossRef]

18. Derjaguin, B.; Landau, L. Theory of stability of strongly charged lyophobic sols and adhesion of strongly charged particles in solutions of electrolytes. *Acta Physicochim. URSS* **1941**, *14*, 633–662.
19. Verwey, E.J.W.; Overbeek, J.T.G. *Theory of the Stability of Lyophobic Colloids*; Elsevier: Amsterdam, The Netherlands, 1948.
20. Russel, W.B.; Saville, D.A.; Schowalter, W.R. *Colloidal Dispersions*; Cambridge University Press: Cambridge, UK, 1989.
21. Gao, X.; Zhu, Z.; Zhang, J.; Wang, J.; Xu, Y. Estimation of the surface potential of clay mineral taking Na+/K+-specific ion effects into account. *Front. Mater.* **2022**, *9*, 943832. [CrossRef]
22. Pignon, F.; Piau, J.M.; Magnin, A. Structure and pertinent length scale of a discotic clay gel. *Phys. Rev. Lett.* **1996**, *76*, 4857–4860. [CrossRef]
23. Morvan, M.; Espinat, D.; Lambard, J.; Zemb, T. Ultrasmall- and small-angle X-ray scattering of smectite clay suspensions. *Colloids Surf. A Physicochem. Eng. Asp.* **1994**, *82*, 193–203. [CrossRef]
24. Kimura, H. Deionization-induced colorless transparency in physical gels formed by clay aqueous dispersions. *Appl. Clay Sci.* **2024**, *249*, 107261. [CrossRef]
25. Kimura, H.; Tanabe, H.; Shinoki, S. Zeta potential as a key indicator of network structure and rheological behavior in smectite clay dispersions. *Fluids* **2025**, *10*, 178. [CrossRef]
26. Kimura, H. Influence of sol–gel state in smectite aqueous dispersions on drying patterns of droplets. *Materials* **2024**, *17*, 2891. [CrossRef]
27. Kimura, H.; Inoue, A. Hierarchy of electrorheological responses in aqueous smectite clay dispersions in relation to DLVO potential barriers. *Eng* **2025**, *6*, 351. [CrossRef]
28. Bonn, D.; Tanaka, H.; Wegdam, G.; Kellay, H.; Meunier, J. Aging of a colloidal "Wigner" glass. *Europhys. Lett.* **1998**, *45*, 52–57. [CrossRef]
29. Mourchid, A.; Levitz, P. Long-term gelation of Laponite aqueous dispersions. *Phys. Rev. E* **1998**, *57*, R4887–R4890. [CrossRef]
30. Cummins, H.Z. Liquid, glass, gel: The phases of colloidal Laponite. *J. Non-Cryst. Solids* **2007**, *353*, 3891–3905. [CrossRef]
31. Abu-Jdayil, B. Rheology of sodium and calcium bentonite–water dispersions: Effect of electrolytes and aging time. *Int. J. Miner. Process.* **2011**, *98*, 208–213. [CrossRef]
32. Au, P.-I.; Leong, Y.-K. Surface chemistry and rheology of Laponite dispersions: Zeta potential, yield stress, ageing, fractal dimension and pyrophosphate. *Appl. Clay Sci.* **2015**, *107*, 36–45. [CrossRef]
33. Leong, Y.K.; Clode, P.L. Time-dependent clay gels: Stepdown shear rate behavior, microstructure, ageing, and phase state ambiguity. *Phys. Fluids* **2023**, *35*, 123329. [CrossRef]
34. Debye, P.; Hückel, E. Zur Theorie der Elektrolyte. I. Gefrierpunktserniedrigung und verwandte Erscheinungen. *Phys. Z.* **1923**, *24*, 185–206.
35. Ohshima, H. A simple expression for Henry's function for the retardation effect in electrophoresis of spherical colloidal particles. *J. Colloid Interface Sci.* **1994**, *168*, 269–271. [CrossRef]
36. Israelachvili, J.N. *Intermolecular and Surface Forces*, 3rd ed.; Academic Press: London, UK, 2011.
37. Kimura, H. Influence of alternating electric fields on the electrorheological effect of aqueous stevensite dispersions. *Appl. Clay Sci.* **2024**, *254*, 107393. [CrossRef]
38. Hogg, R.; Healy, T.W.; Fuerstenau, D.W. Mutual coagulation of colloidal dispersions. *Trans. Faraday Soc.* **1966**, *62*, 1638–1651. [CrossRef]
39. Tadros, T. General principles of colloid stability and the role of surface forces. In *Colloid Stability: The Role of Surface Forces*; Tadros, T.F., Ed.; Wiley-VCH: Weinheim, Germany, 2011; pp. 1–45.
40. Leong, Y.K.; Ong, B.C. Critical zeta potential and the Hamaker constant of oxides in aqueous media. *Powder Technol.* **2003**, *134*, 249–254. [CrossRef]
41. Galli, M.; Sáringer, S.; Szilágyi, I.; Trefalt, G. A simple method to determine critical coagulation concentration from electrophoretic mobility. *Colloids Interfaces* **2020**, *4*, 20. [CrossRef]
42. Gouy, G. Sur la constitution de la charge électrique à la surface d'un électrolyte. *J. Phys. Theor. Appl.* **1910**, *9*, 457–468. [CrossRef]
43. Chapman, D.L. A contribution to the theory of electrocapillarity. *Philos. Mag.* **1913**, *25*, 475–481. [CrossRef]
44. Chang, F.-R.C.; Sposito, G. The electrical double layer of a disk-shaped clay mineral particle: Effects of electrolyte properties and surface charge density. *J. Colloid Interface Sci.* **1996**, *178*, 555–564. [CrossRef]
45. Kitagawa, Y.; Yamaguchi, S.; Yorozu, Y. Effects of sodium chloride concentrations on zeta potentials of clay minerals estimated by an electrokinetic sonic amplitude method. *Clay Sci.* **2003**, *12*, 91–96.
46. Saka, E.E.; Güler, C. The effects of electrolyte concentration, ion species and pH on the zeta potential and electrokinetic charge density of montmorillonite. *Clays Clay Miner.* **2006**, *54*, 853–861. [CrossRef]
47. Dong, Y.; Li, H.; Fan, Y.; Ma, X.; Sun, D.; Wang, Y.; Gao, Z.; Dong, X. Tunable dewatering behavior of montmorillonite suspension by adjusting solution pH and electrolyte concentration. *Minerals* **2020**, *10*, 293. [CrossRef]
48. Winter, H.H.; Chambon, F. Analysis of linear viscoelasticity of a crosslinking polymer at the gel point. *J. Rheol.* **1986**, *30*, 367–382. [CrossRef]

49. Shih, W.H.; Shih, W.Y.; Kim, S.I.; Liu, J.; Aksay, I.A. Scaling behavior of the elastic properties of colloidal gels. *Phys. Rev. A* **1990**, *42*, 4772–4779. [CrossRef]
50. Rueb, C.J.; Zukoski, C.F. Viscoelastic properties of colloidal gels. *J. Rheol.* **1997**, *41*, 197–218. [CrossRef]
51. Ruzicka, B.; Zaccarelli, E. A fresh look at the Laponite phase diagram. *Soft Matter* **2011**, *7*, 1268–1286. [CrossRef]
52. Lifshitz, E.M. The theory of molecular attractive forces between solids. *Sov. Phys. JETP* **1956**, *2*, 73–83.
53. Visser, J. On Hamaker constants: A comparison between Hamaker constants and Lifshitz–van der Waals constants. *Adv. Colloid Interface Sci.* **1972**, *3*, 331–363. [CrossRef]
54. Bergström, L. Hamaker constants of inorganic materials. *Adv. Colloid Interface Sci.* **1997**, *70*, 125–169. [CrossRef]
55. Espinoza, D.N.; Santamarina, J.C. Clay interaction with liquid and supercritical CO_2: The relevance of electrical and capillary forces. *Int. J. Greenh. Gas Control* **2012**, *10*, 351–362. [CrossRef]
56. Weber, C.; Kaufhold, S. Hamaker functions for kaolinite and montmorillonite. *Colloid Interface Sci. Commun.* **2021**, *43*, 100442. [CrossRef]
57. Leite, F.L.; Bueno, C.C.; Da Róz, A.L.; Ziemath, E.C.; Oliveira, O.N., Jr. Theoretical models for surface forces and adhesion and their measurement using atomic force microscopy. *Int. J. Mol. Sci.* **2012**, *13*, 12773–12856. [CrossRef]
58. van Oss, C.J.; Chaudhury, M.K.; Good, R.J. Interfacial Lifshitz–van der Waals and polar interactions in macroscopic systems. *Chem. Rev.* **1988**, *88*, 927–941. [CrossRef]
59. Shen, X.; Bourg, I.C. Molecular dynamics simulations of the colloidal interaction between smectite clay nanoparticles in liquid water. *J. Colloid Interface Sci.* **2021**, *584*, 610–621. [CrossRef]
60. Shen, X.; Bourg, I.C. Interaction between hydrated smectite clay particles as a function of salinity (0–1 M) and counterion type (Na, K, Ca). *J. Phys. Chem. C* **2022**, *126*, 20990–20997. [CrossRef]
61. Tester, C.C.; Aloni, S.; Gilbert, B.; Banfield, J.F. Short- and long-range attractive forces that influence the structure of montmorillonite osmotic hydrates. *Langmuir* **2016**, *32*, 12890–12900. [CrossRef]
62. Christidis, G.E. The concept of layer charge of smectites and its implications for important smectite–water properties. In *Layered Mineral Structures and Their Application in Advanced Technologies*; Brigatti, M.F., Mottana, A., Eds.; EMU Notes in Mineralogy; Mineralogical Society of Great Britain and Ireland: London, UK, 2011; Volume 11, pp. 239–260.
63. Kloprogge, J.T.; Ponce, C.P. Spectroscopic studies of synthetic and natural saponites: A review. *Minerals* **2021**, *11*, 112. [CrossRef]
64. Kleijn, W.B.; Oster, J.D. A model of clay swelling and tactoid formation. *Clays Clay Miner.* **1982**, *30*, 383–390. [CrossRef]

Disclaimer/Publisher's Note: The statements, opinions and data contained in all publications are solely those of the individual author(s) and contributor(s) and not of MDPI and/or the editor(s). MDPI and/or the editor(s) disclaim responsibility for any injury to people or property resulting from any ideas, methods, instructions or products referred to in the content.